applied optics

Modeling, simulation, and fabrication of bi-directional mode-division multiplexing for silicon-on-insulator platform

Omnia M. Nawwar,[1,*] Hossam M. H. Shalaby,[2] and Ramesh K. Pokharel[3]

[1]Department of Electronics and Communications Engineering, Egypt-Japan University of Science and Technology (E-JUST), Alexandria 21934, Egypt
[2]Electrical Engineering Department, Faculty of Engineering, Alexandria University, Alexandria 21544, Egypt
[3]Graduate School of Information Science and Electrical Engineering, Kyushu University, Fukuoka 819-0395, Japan
*Corresponding author: omnia.nawwar@ejust.edu.eg

A strip waveguide-based bi-directional mode-division multiplexer is proposed. A mathematical model has been proposed to analyze the performance, and the results are simulated. The design concept of this device to (de) multiplex three modes simultaneously has been studied previously for slab waveguides, both mathematically using the perturbative mode-coupled theory and by simulation using 2D FDTD Solutions (FDTD, finite difference time domain). As slab waveguides are not suitable for extracting fabrication parameters for most silicon-on-insulator applications, we apply the concept to a more practical device that involves strip waveguides rather than slab waveguides. The effective index method (EIM) has been used to develop the mathematical model and to get approximate forms for both the profiles and coupling coefficients. The return loss of different modes is taken into consideration to fully characterize the device performance. Simple formulas for both insertion and return losses of all multiplexing modes have been derived. In addition, full vectorial 3D FDTD simulations are performed so as to validate our mathematical model. Different design parameters have been used to get numerical results of the proposed device. Our results reveal that the EIM has enough accuracy to characterize the performance of our device compared to that of the complex full vectorial simulation. In order to validate the used model, the device has been fabricated and tested. Good insertion losses and crosstalks for all modes have been obtained. © 2017 Optical Society of America

OCIS codes: (130.3120) Integrated optics devices; (130.2790) Guided waves; (050.2770) Gratings.

https://doi.org/10.1364/AO.57.000042

1. INTRODUCTION

Various multiplexing techniques have been reported to meet the high-bandwidth capacity required for on-chip interconnects [1–4]. By using many light sources at different wavelengths, wavelength-division multiplexing (WDM) techniques have been adopted since the 1980s to make use of the high bandwidth available in optical fiber [2]. The current community goal is to increase the capacity of a single channel in order to increase the aggregate data rate of the network [5–7]. Recently, space-division multiplexing (SDM) has been standing as a promising candidate to achieve the above goal [3,8,9]. In 1979, the first and most obvious SDM approach was reported [10]. Now, it has become an attractive technique for optical interconnects in data centers [3]. Multiple laser sources are hard to realize and manage, which makes WDM not a convenient technique for on-chip communications. Although SDM techniques would use only

one laser source, a multicore-division multiplexing technique still requires a large space, which is a valuable resource for on-chip communications [11,12]. On the other hand, mode-division multiplexing (MDM) techniques have received increasing interest in recent years for on-chip (de)multiplexing, as they reserve both space and laser sources for the system [13]. In MDM, different data streams can be carried by different modes at the same wavelength by engineering the dimensions of the interconnect to support multiple orthogonal modes.

The (de)multiplexer is one of the key components in the MDM system [13–29]. In Ref. [14], a four-mode MDM has been realized using a multimode interference (MMI) coupler with an on-chip area of more than 2 mm². Tapered directional coupler-based MDMs have been proposed in Refs. [18,19]. In Ref. [19], TE_0 and TE_1 (de)multiplexers have been reported with low insertion loss (IL) and crosstalk (–0.3 dB and –16 dB), while the device length is more than 50 µm. In Ref. [18], the

same idea has been reported for TM_0 and TM_1 with short common coupling length for both modes of 15.2 μm and low IL of –0.7 dB. An eight-channel mode (de)multiplexer has been proposed in Ref. [20] using six cascaded directional couplers. The total length of the (de)multiplexer is more than 330 μm. Although the simulated IL for all channels is promising (< – 0.5 dB), the measured IL ranges from –0.2 to –3.5 dB for different modes. A (de)multiplexer has been designed in Ref. [21] that is based on asymmetric Y-junction with length-dependent frequency response. It has been used for two modes with IL less than –1.5 dB and length more than 100 μm. In Ref. [22], a three-mode (de)multiplexer has been proposed. The maximum measured IL is about –5.7 dB at a wavelength of 1550 nm, and the worst crosstalk is –9.5 dB. The length of the (de)multiplexer for the three modes is more than 350 μm. In Ref. [25], an add/drop MDM for both TE_0 and TE_1 has been proposed, which is based on a Mach–Zehnder interferometer assisted with a periodic structure on the arms. The IL for both modes is less than 1 dB, while the length is more than 100 μm. Another add/drop MDM has been proposed in Ref. [30] using two waveguides and a Bragg grating.

Y-junction- and MMI-based MDMs cannot conveniently accommodate more than two modes and require high fabrication tolerance and complex design. Tapered directional couplers-based MDMs are intrinsically limited in bandwidth. However, some studies have been done to increase the bandwidth and reduce the sensitivity to fabrication errors [23,31]. In Ref. [29], a three-mode (de)multiplexer has been proposed based on two slab waveguides and a Bragg grating. It has been referred to as a bidirectional mode-division multiplexer (BMDM). The device concept has been verified both mathematically and with the aid of 2D FDTD simulations. However, a slab concept is not always suitable for extracting parameters for silicon-on-insulator (SOI) fabrication process.

In this paper, we use strip waveguides to provide practical insights to the performance of the BMDM assisted with 3D FDTD simulation. We develop a mathematical model to study the performance of the BMDM with strip waveguides. The rigorous analysis makes it possible to design the device at any wavelength, for any modes, and for any waveguide dimensions by using only the final equations. Specifically, the mode profiles for all involved modes in a strip waveguide are written using the effective index method (EIM). The EIM has proven to be in good agreement with full vectorial methods, yet is much simpler [32–36]. In Ref. [32], the implementation of EIM has been proven to be applicable to a wide range of guiding structures (strip, buried, and diffused guides) and has been tested against analytical solutions and against other methods' results to prove good agreement. Using this method, a 2D problem is transformed into 1D problems (slab) that are easy to express. The first slab is in the horizontal direction and has a thickness as the height of the strip waveguide. The second slab is in the vertical direction and has a height as the width of the strip waveguide. The vertical slab uses modes resulted from solving the horizontal slab. In addition, we drive approximated expressions for different coupling coefficients in the strip waveguide using perturbative coupled-mode theory. The return loss (RL) in the input waveguide due to the existence of Bragg grating is taken into account in our analysis to fully characterize the device. Expressions for both the ILs and crosstalks are obtained and examined for different device parameters. Furthermore, a 3D FDTD simulation is provided to ensure the consistency between our mathematical model and a 3D vectorial method. The dispersion of the silicon is not taken into account in the theoretical analysis for simplicity; however, it is taken into account in the 3D FDTD simulation. Finally, the device is fabricated and tested to validate the used model. The IL of the proposed device ranges from –0.5 to –5.4 dB for different modes with a length of only 18 μm. Compared to other MDMs mentioned in literature for more than two modes, our device has about 10-fold reduction in size [14,20,22] and easy to be extended to higher-order modes.

The remaining of this paper is organized as follows. Mode profiles of the proposed structure are presented in Section 2. It includes the normalization factors for the modes and orthogonality property. Section 3 is devoted to the development of the coupled-mode equations for both forward- and backward-propagating modes in both device waveguides. The solutions to these equations are provided in Section 4. 3D FDTD simulations based on our numerical results are presented in Section 5 along with some parametric studies. The fabrication process is described in Section 6. The experimental data are analyzed to get the ILs and crosstalks for all modes. The experimental results are presented in the same section. Finally, our conclusions are given in Section 7.

2. DEVICE STRUCTURE AND MODE PROFILES

The structure of the proposed BMDM (de)multiplexer is illustrated in Fig. 1 with the origin of the axes at the center of the input facet of the lower waveguide.

It consists of two strip waveguides and a Bragg grating in between. One of the waveguides is a multimode (also called input) waveguide of width w, while the other is a single-mode (also called output) waveguide of width d. Port 1 represents the input port where three modes are launched: TE_0, TE_1, and TE_2. The fundamental mode TE_0 is kept in the input waveguide and propagates to port 2. The first-order mode TE_1 couples via a traditional directional coupler to the output waveguide and propagates forward to port 3, while the second-order mode TE_2 couples via the Bragg grating and propagates backward to port 4. Every tooth from the Bragg grating diffracts a small amount of the second-order mode to the output waveguide, causing the coupling in the backward direction. The height of both waveguides is h, and the device length is L. The grating period is Λ, and the teeth width is $t \leq r$, where r is the coupler gap.
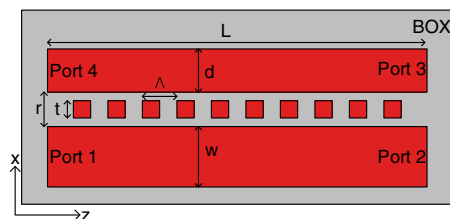

Fig. 1. Structure of proposed BMDM with strip waveguides.

By inserting a Bragg grating between the two waveguides, every waveguide would see a different perturbation to the refractive index. The perturbation $\Delta n_{\text{multi}}^2(x, y, z)$ seen by the input waveguide can be obtained by subtracting the unperturbed index from the total index of the system. This can be written as a series of rectangles and expanded using Fourier series [29]. For any $h \geq y \geq 0$ and any $z \geq 0$, we have for $L \gg \Lambda$:

$$\Delta n_{\text{multi}}^2(x, y, z)$$
$$= \begin{cases} 2b_0; & |x - w/2 - r - d/2| \leq d/2, \\ \sum_{\nu=-\infty}^{\infty} b_\nu e^{-j\nu(2\pi/\Lambda)z}; & |x - w/2 - r/2| \leq t/2, \\ 0; & \text{elsewhere}, \end{cases} \quad \textbf{(1)}$$

where

$$b_\nu = \frac{n_1^2 - n_2^2}{2} \text{sinc}(\nu/2), \qquad \nu \in \{\ldots, -1, 0, 1, \ldots\}. \quad \textbf{(2)}$$

Here, n_1 and n_2 are the refractive indices for the waveguide material and its surroundings, respectively, and ν is the grating order. A similar expression can be deduced for the output waveguide: for any $h \geq y \geq 0$ and any $z \geq 0$,

$$\Delta n_{\text{single}}^2(x, y, z)$$
$$= \begin{cases} 2b_0; & |x| \leq w/2, \\ \sum_{\nu=-\infty}^{\infty} b_\nu e^{-j\nu(2\pi/\Lambda)z}; & |x - w/2 - r/2| \leq t/2, \\ 0; & \text{elsewhere}. \end{cases} \quad \textbf{(3)}$$

A. Mode Profiles

In this subsection, we use EIM to express the 2D mode profiles of our BMDM (de)multiplexer. EIM converts original 3D channel waveguides into effective 2D planar waveguides, which is easy to be studied analytically. The profiles are written as $\Psi(x, y) = G(y)F(x)$, where $G(y)$ and $F(x)$ are the electric fields of two slab waveguides in y and x directions, respectively. Since the heights of both input and output waveguides are the same, their electric fields in y direction are the same as well:

$$G(y) = \begin{cases} A \cos(\phi)e^{\gamma y}; & \text{if } y < 0, \\ A \cos(\rho y - \phi); & \text{if } h \geq y \geq 0, \\ A \cos(\rho h - \phi)e^{-\gamma(y-h)}; & \text{if } y > h, \end{cases} \quad \textbf{(4)}$$

where A is a constant. The parameters ρ, γ, and ϕ are given by

$$\rho = \frac{2\pi}{\lambda_0} \sqrt{n_1^2 - n_{\text{eff}_g}^2}$$
$$\gamma = \frac{2\pi}{\lambda_0} \sqrt{n_{\text{eff}_g}^2 - n_2^2}$$
$$\phi = \tan^{-1} \frac{\gamma}{\rho}. \quad \textbf{(5)}$$

Here, n_{eff_g} is the effective index of a slab waveguide of height h in y direction, and λ_0 is the operating wavelength. In x direction, the electric fields are different, as both waveguides have different widths:

$$F_m(x)$$
$$= \begin{cases} \frac{N_{\text{wg}_m} \eta_0}{n_2^2} C_m \cos(\alpha_m w/2 + m\pi/2) \cdot e^{\sigma_m(x+w/2)}; & \text{if } x < -w/2, \\ \frac{N_{\text{wg}_m} \eta_0}{n_{\text{eff}_g}^2} C_m \cos(\alpha_m x - m\pi/2); & \text{if } |x| \leq w/2, \\ \frac{N_{\text{wg}_m} \eta_0}{n_2^2} C_m \cos(\alpha_m w/2 - m\pi/2) \cdot e^{-\sigma_m(x-w/2)}; & \text{if } x > w/2, \end{cases}$$
$$\textbf{(6)}$$

$$F_s(x)$$
$$= \begin{cases} \frac{N_{\text{wg}_s} \eta_0}{n_2^2} C_s \cos(\alpha_s d/2) \cdot e^{\sigma_s(x-w/2-r)}; & \text{if } x < w/2 + r, \\ \frac{N_{\text{wg}_s} \eta_0}{n_{\text{eff}_g}^2} C_s \cos[\alpha_s(x - w/2 - r - d/2)]; & \text{if } |x - \frac{w}{2} - r - \frac{d}{2}| \leq d/2, \\ \frac{N_{\text{wg}_s} \eta_0}{n_2^2} C_s \cos(\alpha_s d/2) \cdot e^{-\sigma_s(x-w/2-r-d)}; & \text{if } x > w/2 + r + d, \end{cases}$$
$$\textbf{(7)}$$

where $F_m(x)$ and $F_s(x)$ are the fields for input and output waveguides, respectively. η_0 is wave impedance in free space defined as $\sqrt{\mu_0/\epsilon_0}$ where μ_0 and ϵ_0 are free-space permeability and permittivity, respectively. Here, $m \in \{0, 1, 2\}$ denotes the mode order in the input multimode waveguide, while s labels the output single-mode waveguide. For any $i \in \{s, 0, 1, 2\}$, N_{wg_i} is the final effective index of the waveguide. In addition, α_i and σ_i are given by

$$\alpha_i = \frac{2\pi}{\lambda_0} \sqrt{n_{\text{eff}_g}^2 - N_{\text{wg}_i}^2}$$
$$\sigma_i = \frac{2\pi}{\lambda_0} \sqrt{N_{\text{wg}_i}^2 - n_2^2}, \quad \textbf{(8)}$$

respectively. The constants A and C_i are chosen so that power flow in z direction is unity. Using Eqs. (4), (6), and (7), we can extract the orthogonality property for strip waveguides:

$$\iint \Psi_n^*(x, y)\Psi_m(x, y) \mathrm{d}x \mathrm{d}y = \frac{2\eta_0^2 N_{\text{wg}_n}}{n_{\text{eff}_g}} \delta_{\text{nm}}, \quad \textbf{(9)}$$

where δ_{nm} is the Kronecker delta.

3. COUPLED-MODE EQUATIONS

In this section, we aim at finding a system of first-order coupled differential equations that relates the amplitudes of the forward- and backward-propagating modes for the input and output waveguides using coupled-mode theory. The electric field in the coupling region can be expressed as a superposition of the unperturbed fields of both waveguides with amplitude perturbation:

$$E(x, y, z) = \sum_{m=0}^{2} (\mathcal{A}_m^+(z)e^{-j\beta_m z} + \mathcal{A}_m^-(z)e^{j\beta_m z})\Psi_m(x, y)$$
$$+ (\mathcal{B}^+(z)e^{-j\beta_s z} + \mathcal{B}^-(z)e^{j\beta_s z})\Psi_s(x, y), \quad \textbf{(10)}$$

where $\mathcal{A}_m^{\pm}(z)$ and $\mathcal{B}^{\pm}(z)$ are complex amplitudes of mode m in the input waveguide and the fundamental mode in the output waveguide, respectively. In addition, $\Psi_i(x, y)$ is the electric field profile for mode $i \in \{s, 0, 1, 2\}$, and $\beta_i(z) = 2\pi N_{\text{wg}_i}/\lambda_0$

denotes its propagation constant. We start from the wave equation for perturbed and unperturbed systems and follow the procedures in Refs. [37,38] to get

$$
\sum_{m=0}^{2} -2j\beta_m \left(\frac{d\mathcal{A}_m^+(z)}{dz} e^{-j\beta_m z} - \frac{d\mathcal{A}_m^-(z)}{dz} e^{j\beta_m z} \right) \Psi_m(x,y)
$$

$$
- 2j\beta_s \left(\frac{d\mathcal{B}^+(z)}{dz} e^{-j\beta_s z} - \frac{d\mathcal{B}^-(z)}{dz} e^{j\beta_s z} \right) \Psi_s(x,y)
$$

$$
= -k_0^2 \Bigg[\sum_{m=0}^{2} (\mathcal{A}_m^+(z) e^{-j\beta_m z} + \mathcal{A}_m^-(z) e^{j\beta_m z})
$$

$$
\times \Delta n_{\text{multi}}^2(x,y,z) \Psi_m(x,y)
$$

$$
+ (\mathcal{B}^+(z) e^{-j\beta_s z} + \mathcal{B}^-(z) e^{j\beta_s z}) \Delta n_{\text{single}}^2(x,y,z) \Psi_s(x,y) \Bigg]. \quad \textbf{(11)}
$$

From the last equation, we derive coupled-mode equations for both $\mathcal{A}_m^\pm(z)$ and $\mathcal{B}^\pm(z)$, as discussed in the following subsections.

A. Coupled-Mode Equation for Input Waveguide Modes

Multiplying Eq. (11) by $\Psi_n^*(x,y)$, integrating over both x and y, and using orthogonality property Eq. (9), we get the coupled-mode equation for $\mathcal{A}_n^+(z)$:

$$
\frac{d\mathcal{A}_n^+(z)}{dz}
$$

$$
= -j \frac{\omega\epsilon_0}{4\eta_0} \frac{n_{\text{eff}_g}}{N_{\text{wg}_n^2}} \Bigg\{ \sum_\nu b_\nu \Bigg(\sum_{m=0}^{2} [\mathcal{A}_m^+(z) e^{-j(\beta_m - \beta_n + 2\pi\nu/\lambda)z}
$$

$$
+ \mathcal{A}_m^-(z) e^{j(\beta_m + \beta_n - 2\pi\nu/\lambda)z}]
$$

$$
\times \iint_{\substack{h \ge y \ge 0 \\ |x - w/2 - r/2| \le t/2}} \Psi_n^*(x,y) \Psi_m(x,y) dx dy
$$

$$
+ [\mathcal{B}^+(z) e^{-j(\beta_s - \beta_n + 2\pi\nu/\lambda)z} + \mathcal{B}^-(z) e^{j(\beta_s + \beta_n - 2\pi\nu/\lambda)z}]
$$

$$
\times \iint_{\substack{h \ge y \ge 0 \\ |x - w/2 - r/2| \le t/2}} \Psi_n^*(x,y) \Psi_s(x,y) dx dy \Bigg)
$$

$$
+ 2b_0 \mathcal{B}^+(z) e^{-j(\beta_s - \beta_n)z} \cdot \iint_{\substack{h \ge y \ge 0 \\ |x| \le w/2}} \Psi_n^*(x,y) \Psi_s(x,y) dx dy \Bigg\},
$$

$$
\textbf{(12)}
$$

where $\Delta n_{\text{multi}}(x,y,z)$ and $\Delta n_{\text{single}}(x,y,z)$ have been substituted from Eq. (1) and Eq. (3), respectively. In addition, ω is the angular frequency. We study Eq. (12) for $n \in \{1,2\}$ to get the forward-propagating modes. In order to couple the first-order mode HE_{21} of the input waveguide to the fundamental mode of the output waveguide, both propagation constants should be equal. The second-order mode TE_2 of the input waveguide would couple contra-directionally via the grating to the fundamental mode of the output waveguide. The corresponding phase-matching conditions are

$$
\beta_1 = \beta_s
$$

$$
\beta_2 + \beta_s = \frac{2\pi}{\Lambda}. \quad \textbf{(13)}
$$

Applying these constraints to Eq. (12) and neglecting phase unmatched terms, we get the coupled equations for $\mathcal{A}_n^+(z)$, $n \in \{1,2\}$:

$$
\frac{d\mathcal{A}_1^+(z)}{dz} = -j\{\xi_{11}^0 \mathcal{A}_1^+(z) + \xi_{12}^1 \mathcal{A}_2^-(z) + (\kappa_1^0 + \varsigma_1)\mathcal{B}^+(z)\}
$$

$$
\frac{d\mathcal{A}_2^+(z)}{dz} = -j\{\xi_{22}^0 \mathcal{A}_2^+(z) + \xi_{21}^1 \mathcal{A}_1^-(z) + \kappa_2^1 \mathcal{B}^-(z)\}, \quad \textbf{(14)}
$$

where for any $n, m \in \{1,2\}$ and any $\nu \in \{0,1\}$, ξ_{nm}^ν, κ_n^ν, and ς_n are coupling coefficients defined over different regions of the proposed (de)multiplexer. Their values depend on the overlap of different fields within the dielectric perturbation. Specifically:

$$
\xi_{nm}^\nu = \frac{\omega\epsilon_0}{4\eta_0} \frac{n_{\text{eff}_g}}{N_{\text{wg}_n^2}} b_\nu \iint_{\substack{h \ge y \ge 0 \\ |x - w/2 - r/2| \le t/2}} \Psi_n^*(x,y) \Psi_m(x,y) dx dy
$$

$$
= a_{nm}^\nu \cdot \left(\frac{h}{2} + \frac{\gamma}{\gamma^2 + \rho^2} \right) \cdot \frac{1}{\sigma_n + \sigma_m} e^{-r/2(\sigma_n + \sigma_m)}
$$

$$
\times 2 \sinh\left[\frac{t}{2}(\sigma_n + \sigma_m) \right],
$$

$$
\kappa_n^\nu = \frac{\omega\epsilon_0}{4\eta_0} \frac{n_{\text{eff}_g}}{N_{\text{wg}_n^2}} b_\nu \iint_{\substack{h \ge y \ge 0 \\ |x - w/2 - r/2| \le t/2}} \Psi_n^*(x,y) \Psi_s(x,y) dx dy
$$

$$
= c_n^\nu \cdot \left(\frac{h}{2} + \frac{\gamma}{\gamma^2 + \rho^2} \right) \cdot \frac{1}{\sigma_n - \sigma_s} e^{-r/2(\sigma_n + \sigma_s)}
$$

$$
\times 2 \sinh\left[\frac{t}{2}(\sigma_n - \sigma_s) \right],
$$

$$
\varsigma_n = \frac{\omega\epsilon_0}{4\eta_0} \frac{n_{\text{eff}_g}}{N_{\text{wg}_n^2}} \cdot 2b_0 \iint_{\substack{h \ge y \ge 0 \\ |x| \le w/2}} \Psi_n^*(x,y) \Psi_s(x,y) dx dy
$$

$$
= d_n^0 \cdot \left(\frac{h}{2} + \frac{\gamma}{\gamma^2 + \rho^2} \right) \cdot \frac{\alpha_n e^{-\sigma_s r}}{(\alpha_n^2 + \sigma_s^2)\sqrt{\sigma_n^2 + \alpha_n^2}}
$$

$$
\cdot [\sigma_s(1 - e^{-\sigma_s w}) + \sigma_n(1 + e^{\sigma_s w})], \quad \textbf{(15)}
$$

where

$$
a_{nm}^\nu \overset{\text{def}}{=} \frac{\omega\epsilon_0}{4\eta_0} \frac{n_{\text{eff}_g}}{N_{\text{wg}_n^2}} b_\nu \cdot A^2 \frac{N_{\text{wg}_n}\eta_0}{n_2^2} C_n \cos(\alpha_n w/2 - n\pi/2)
$$

$$
\times \frac{N_{\text{wg}_m}\eta_0}{n_2^2} C_m \cos(\alpha_m w/2 - m\pi/2)
$$

$$
c_n^\nu \overset{\text{def}}{=} \frac{\omega\epsilon_0}{4\eta_0} \frac{n_{\text{eff}_g}}{N_{\text{wg}_n^2}} b_\nu \cdot A^2 \frac{N_{\text{wg}_n}\eta_0}{n_2^2} C_n \cos(\alpha_n w/2 - n\pi/2)
$$

$$
\times \frac{N_{\text{wg}_s}\eta_0}{n_2^2} C_s \cos(\alpha_s d/2)
$$

$$
d_n^0 \overset{\text{def}}{=} \frac{\omega\epsilon_0}{4\eta_0} \frac{n_{\text{eff}_g}}{N_{\text{wg}_n^2}} \cdot 2b_0 \cdot A^2 \frac{N_{\text{wg}_n}\eta_0}{n_{\text{eff}_g}^2} C_n \times \frac{N_{\text{wg}_s}\eta_0}{n_2^2} C_s \cos(\alpha_s d/2).
$$

$$
\textbf{(16)}
$$

It should be remarked that the inter-waveguide coupling coefficient κ is a parameter of most interest to device performance. Indeed, it controls the coupling from the input waveguide to the output waveguide through the grating in both forward and backward directions.

Following the same procedure as in the last subsection, we get $\frac{d\mathcal{A}_n(z)}{dz}$, $n \in \{1, 2\}$:

$$\frac{d\mathcal{A}_1^-(z)}{dz} = j\{\xi_{11}^0 \mathcal{A}_1^-(z) + \xi_{12}^1 \mathcal{A}_2^+(z) + (\kappa_1^0 + \varsigma_1)\mathcal{B}^-(z)\}$$

$$\frac{d\mathcal{A}_2^-(z)}{dz} = j\{\xi_{22}^0 \mathcal{A}_2^-(z) + \xi_{21}^1 \mathcal{A}_1^+(z) + \kappa_2^1 \mathcal{B}^+(z)\}. \tag{17}$$

Both Eqs. (14) and (17) indicate that the back-reflection in the input waveguide is directly related to ξ_{12}^1 or ξ_{21}^1.

B. Coupled-Mode Equation for Output Waveguide Mode

Again, multiplying Eq. (11) by $\Psi_s^*(x, y)$, integrating over x and y, and using the orthogonality property, we get

$$\frac{d\mathcal{B}^+(z)}{dz} = -j\{(\kappa_1^0 + \varpi_1)\mathcal{A}_1^+(z) + \kappa_2^1 \mathcal{A}_2^-(z) + \iota^0 \mathcal{B}^+(z)\}, \tag{18}$$

where ι^ν and ϖ_n are new coupling coefficients defined as

$$\iota^\nu = \frac{\omega\epsilon_0}{4\eta_0} \frac{n_{\text{eff}_g}}{N_{\text{wg}_s^2}} . b_\nu \iint\limits_{\substack{h \geq y \geq 0 \\ |x-w/2-r/2| \leq t/2}} \Psi_s^*(x, y)\Psi_s(x, y) dx dy$$

$$= f^\nu \cdot \left(\frac{h}{2} + \frac{\gamma}{\gamma^2 + \rho^2}\right) \cdot e^{-r\sigma_s} \cdot \frac{\sinh(t\sigma_s)}{\sigma_s}$$

$$\varpi_n = \frac{\omega\epsilon_0}{4\eta_0} \frac{n_{\text{eff}_g}}{N_{\text{wg}_s^2}} . 2b_0 \iint\limits_{\substack{h \geq y \geq 0 \\ |x-w/2-r-d/2| \leq d/2}} \Psi_s^*(x, y)\Psi_n(x, y) dx dy$$

$$= g_n^0 \cdot \left(\frac{h}{2} + \frac{\gamma}{\gamma^2 + \rho^2}\right) \cdot \frac{\alpha_s e^{-\sigma_n r}}{(\alpha_s^2 + \sigma_n^2)\sqrt{\sigma_s^2 + \alpha_s^2}}$$

$$\cdot [\sigma_s(1 + e^{-\sigma_n d}) + \sigma_n(1 - e^{-\sigma_n d})], \tag{19}$$

where

$$f^\nu \overset{\text{def}}{=} \frac{\omega\epsilon_0}{4\eta_0} \frac{n_{\text{eff}_g}}{N_{\text{wg}_s^2}} b_\nu \cdot A^2 \left(\frac{N_{\text{wg}_s}\eta_0}{n_2^2} C_s \cos(\alpha_s d/2)\right)^2$$

$$g_n^0 \overset{\text{def}}{=} \frac{\omega\epsilon_0}{4\eta_0} \frac{n_{\text{eff}_g}}{N_{\text{wg}_s^2}} \cdot 2b_0 \cdot A^2 \frac{N_{\text{wg}_s}\eta_0}{n_{\text{eff}_g^2}} C_s$$

$$\times \frac{N_{\text{wg}_s}\eta_0}{n_2^2} C_n \cos(\alpha_n w/2 - n\pi/2). \tag{20}$$

Similar to ς_n, ϖ_n quantifies the intra-waveguide coupling in the output waveguide. Finally, we can get the coupled-mode equation for $\mathcal{B}^-(z)$ as

$$\frac{d\mathcal{B}^-(z)}{dz} = j\{(\kappa_1^0 + \varpi_1)\mathcal{A}_1^-(z) + \kappa_2^1 \mathcal{A}_2^+(z) + \iota^0 \mathcal{B}^-(z)\}. \tag{21}$$

4. SOLUTION OF COUPLED-MODE EQUATIONS

To solve the system of differential equations described by Eqs. (14), (17), (18), and (21), we need to introduce a phase correction term to phase-matching conditions in Eq. (13):

$$\beta_1 + \xi_{11}^0 = \beta_s + \iota^0$$

$$\beta_2 + \xi_{22}^0 + \beta_s + \iota^0 = \frac{2\pi}{\Lambda}. \tag{22}$$

Accordingly, the grating period is determined as

$$\Lambda = \left[\frac{N_{\text{wg}_2} + N_{\text{wg}_s}}{\lambda_0} + \frac{\xi_{22}^0 + \iota^0}{2\pi}\right]^{-1}. \tag{23}$$

The new mode amplitudes are defined as

$$\mathcal{A}_1^+(z) = \mathcal{C}_1^+(z)e^{-j\xi_{11}^0 z} \qquad \mathcal{A}_1^-(z) = \mathcal{C}_1^-(z)e^{j\xi_{11}^0 z}$$

$$\mathcal{A}_2^+(z) = \mathcal{C}_2^+(z)e^{-j\xi_{22}^0 z} \qquad \mathcal{A}_2^-(z) = \mathcal{C}_2^-(z)e^{j\xi_{22}^0 z}$$

$$\mathcal{B}^+(z) = \mathcal{D}^+(z)e^{-j\iota^0 z} \qquad \mathcal{B}^-(z) = \mathcal{D}^-(z)e^{j\iota^0 z}. \tag{24}$$

The new set of coupled-mode equations are thus

$$\frac{d\mathcal{C}_1^+(z)}{dz} = -j\{\xi_{12}^1 e^{j(\xi_{11}^0 + \xi_{22}^0)z}\mathcal{C}_2^-(z) + (\kappa_1^0 + \varsigma_1)e^{-j(\iota^0 - \xi_{11}^0)z}\mathcal{D}^+(z)\}$$

$$\frac{d\mathcal{C}_2^+(z)}{dz} = -j\{\xi_{21}^1 e^{j(\xi_{11}^0 + \xi_{22}^0)z}\mathcal{C}_1^-(z) + \kappa_2^1 e^{j(\iota^0 + \xi_{22}^0)z}\mathcal{D}^-(z)\}$$

$$\frac{d\mathcal{D}^+(z)}{dz} = -j\{(\kappa_1^0 + \varpi_1)e^{j(\iota^0 - \xi_{11}^0)z}\mathcal{C}_1^+(z) + \kappa_2^1 e^{j(\iota^0 + \xi_{22}^0)z}\mathcal{C}_2^-(z)\}$$

$$\frac{d\mathcal{C}_1^-(z)}{dz} = j\{\xi_{12}^1 e^{-j(\xi_{11}^0 + \xi_{22}^0)z}\mathcal{C}_2^+(z) + (\kappa_1^0 + \varsigma_1)e^{j(\iota^0 - \xi_{11}^0)z}\mathcal{D}^-(z)\}$$

$$\frac{d\mathcal{C}_2^-(z)}{dz} = j\{\xi_{21}^1 e^{-j(\xi_{11}^0 + \xi_{22}^0)z}\mathcal{C}_1^+(z) + \kappa_2^1 e^{-j(\iota^0 + \xi_{22}^0)z}\mathcal{D}^+(z)\}$$

$$\frac{d\mathcal{D}^-(z)}{dz} = j\{\kappa_2^1 e^{-j(\iota^0 + \xi_{22}^0)z}\mathcal{C}_2^+(z) + (\kappa_1^0 + \varpi_1)e^{-j(\iota^0 - \xi_{11}^0)z}\mathcal{C}_1^-(z)\}. \tag{25}$$

These equations indicate that some unavoidable back-reflections exist. The first-order mode $\mathcal{C}_1^+(z)$ not only couples to the forward direction of the output waveguide $\mathcal{D}^+(z)$, but also to the second-order mode in the backward direction of the same waveguide $\mathcal{C}_2^-(z)$. The second-order mode experiences the same effect by coupling into the first-order mode in the backward direction of the same waveguide. This system of differential equations can be written in a matrix form:

$$\frac{dE(z)}{dz} = S_1(z)E(z), \tag{26}$$

where

$$E(z) = \begin{bmatrix} E^+(z) \\ E^-(z) \end{bmatrix} = \begin{bmatrix} \mathcal{C}_1^+(z) \\ \mathcal{C}_2^+(z) \\ \mathcal{D}^+(z) \\ \mathcal{C}_1^-(z) \\ \mathcal{C}_2^-(z) \\ \mathcal{D}^-(z) \end{bmatrix}, \tag{27}$$

and $S_1(z)$ is the coefficient matrix. To solve this system of differential equations, we define another matrix $S_2(z) = \int_0^z S_1(\tau)d\tau$ and make sure it commutes with $S_1(z)$. The solution will be in the form of $E(L) = \phi(L)E(z_0)$. In addition, we introduce some transformation to $\phi(L)$ to get the solution in the form

$$\begin{bmatrix} E^+(L) \\ E^-(0) \end{bmatrix} = M(L)\begin{bmatrix} E^+(0) \\ E^-(L) \end{bmatrix}, \tag{28}$$

where $M(L)$ is the transformed matrix.

5. NUMERICAL RESULTS AND 3D FDTD SIMULATION

In this subsection, we use our developed theoretical expressions to determine the device parameters to be used in 3D FDTD simulations. First, we plot the mode chart for a strip waveguide

of height 220 nm, provided by most foundries, from which we choose a proper width for both waveguides to support the desired modes and satisfy the phase-matching conditions. The equations from the previous section would help in characterizing our proposed device. Next, we feed chosen parameters to a 3D FDTD simulation in order to verify our mathematical model. The challenge here is to design a BMDM that has good performance for both first- and second-order modes simultaneously.

A. Choosing Dimensions of Waveguides

The mode chart of a strip waveguide is illustrated in Fig. 2 for a height of 220 nm and a wavelength of 1550 nm using the full vectorial method. The polarization of each mode and its profile, calculated using the EIM at the desired width, are indicated in the same figure. The EIM has been used to get the effective indices and profiles for all modes, which are used later to calculate all coupling coefficients from Eqs. (15) and (19). The vertical dotted lines indicate the dimensions of the input and output waveguides. The upper horizontal line has two intersections, which represent the phase-matching conditions between the first-order mode in the input waveguide and the fundamental mode in the output waveguide. For both modes to couple co-directionally, they are supposed to have the same phase. The lower horizontal line represents the effective index of the second-order mode in the input waveguide, which is used to calculate the period of the Bragg grating. The output waveguide is selected to have a width of $d = 450$ nm. Using EIM, the fundamental mode has an effective index of
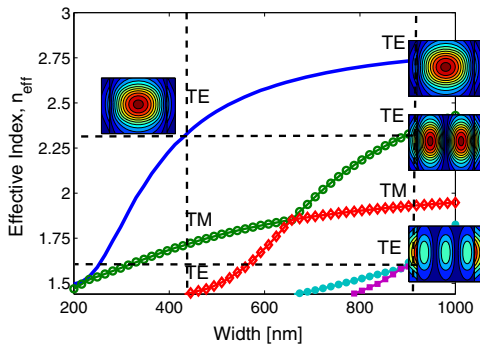

Fig. 2. Strip waveguide mode chart of 220 nm height and 1550 nm wavelength.

$N_{wg_s} = 2.4109$. The width of the input waveguide is selected to support the first three TE-like modes, $w = 936$ nm. For TE_0, TE_1, and TE_2 the EIM gives effective indices of $N_{wg_0} = 2.7316$, $N_{wg_1} = 2.3833$, and $N_{wg_2} = 1.7747$, respectively. The discrepancies between the full vectorial method and EIM are 0.38%, 0.73%, and 5.39% for the three modes. This result is expected, as the EIM is most suited for lower-order modes.

B. Choosing Gap

The coupling gap is chosen so that the inter-waveguide coupling coefficients are high enough to guarantee the highest coupling between both waveguides. In Fig. 3(a), we plot various coupling coefficients, κ_1^0, κ_2^1, ς_1, ϖ_1, and ξ_{12}^1, versus the gap. From Eqs. (15) and (19), we can describe each coupling coefficient as follows. ξ and ι represent the intra-waveguide coupling due to the existence of the Bragg grating in the input and output waveguides, respectively. ς and ϖ represent the interaction between modes from both waveguides over the input and output waveguides, respectively. As ς and ϖ represent the interaction between modes from different waveguides, they are monotonically dependent on the gap. The inter-waveguide coupling κ increases with the coupler gap until a maximum value then decreases again. Indeed, for small values of the coupler gap, many rays would miss the introduced perturbation, and κ becomes small. On the other hand, as the gap increases, more rays would see the perturbation, and the interaction with the grating teeth would increase. As the gap increases further, both waveguides will be separated enough to reduce the coupling between them, and, accordingly, κ would decrease. As the ILs for both modes are functions of the coupling coefficients, they will be functions of the gap. For the first-order mode, IL decreases as the gap increases because rays miss the other waveguide. For the second-order mode, IL will increase with the gap as the rays see more perturbation (tooth depth). After a certain value, IL will decrease again because rays miss the other waveguide. It is also clear from the figure that ξ_{12}^1, which is a main contributor to the back reflection, increases with the gap. Indeed, as the gap increases, the two waveguides are separated enough to prevent inter-waveguide coupling. Accordingly, back reflection would increase. For further gap increase, ξ_{12}^1 reaches its maximum steady value and the back reflection cannot increase any more. The peaks of κ_1^0 and κ_2^1 are calculated to be 3.265×10^{-5} nm^{-1} and 8.424×10^{-5} nm^{-1}, respectively. Choosing the coupling gap as 140 nm ensures that the IL would be minimized for both modes at the same time.
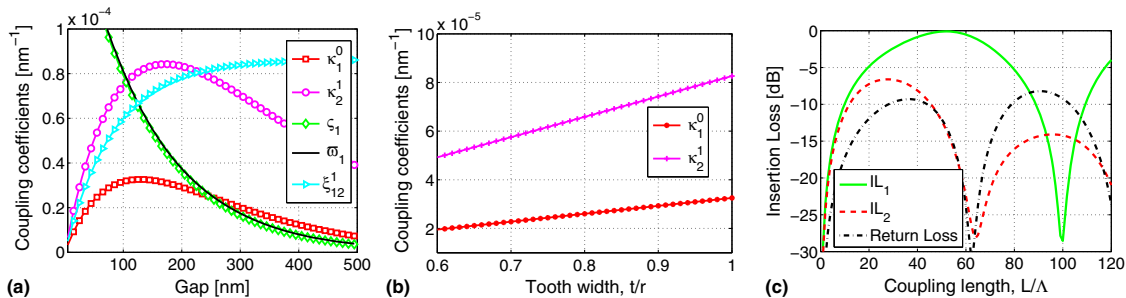

Fig. 3. (a) Various coupling coefficients for tooth width $t = r$. (b) Inter-waveguide coupling coefficients as functions of tooth width t. (c) IL and RL for both first- and second-order modes at $r = 140$ nm.

The corresponding period can be calculated from Eq. (23) to be 364.4 nm for $t = r$. Another parameter that affects inter-waveguide coupling coefficients is the tooth width t. Figure 3(b) shows a monotonic dependence of κ on the tooth width. To get the highest coupling value, we choose $t = r$ for subsequent simulations.

C. Insertion Loss and Return loss

The ILs and RLs for first- and second-order modes are plotted versus the coupling length in Fig. 3(c) for a coupler gap of 140 nm. As the first-order mode couples via the traditional directional coupler, it has a periodic behavior with constructive and destructive interference points. The second-order mode has damping oscillations with the length. This is a direct result of the increase in the reflected power as the length increases. The RL is almost the same in the case of first- or second-order mode excitations. This RL value cannot be suppressed, as it is a direct result of the existence of the Bragg grating. In order to achieve good IL for both modes and a compact device length simultaneously, we choose the device length at the first peak of IL_2, $30\,\Lambda$.

D. 3D FDTD Simulation

In this subsection, we use the obtained values for the (de)multiplexer's parameters from the last subsections to perform 3D FDTD simulations. In our simulation, we uses a 220 nm height strip waveguide with SiO_2 cladding and BOX of 2 μm. Since we are studying the performance of the device for different wavelengths, the refractive index-wavelength dependence of Si and SiO_2 are taken into account. A Lorentzian model has been used in our simulation to fit the silicon data from Palik's handbook [39]. The coupler gap, grating period, and length are chosen to be 140 nm, 364.4 nm, and $30\,\Lambda$, respectively. Figure 4 shows the resulting ILs and crosstalks versus wavelength for each of the excited three modes. In addition, the RLs versus wavelengths for both first- and second-order modes are plotted in the insets of Figs. 4(b) and 4(c), respectively. It is clear from these two insets
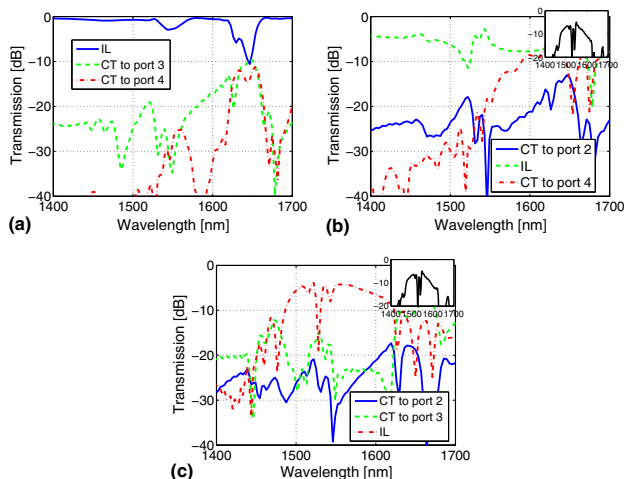
that the RLs are almost the same, which is consistent with our mathematical model.

At 1550 nm, the ILs for the fundamental, first-, and second-order modes are –2.76 dB, –5.402 dB, and –4.2002 dB, respectively. It is worth noting that the IL of the first-order mode can be reduced further by operating at a slightly different wavelength. Specifically, at 1543 nm, the IL of this mode would be reduced to –2.744 dB [Fig. 4(b)]. Accordingly, our device can be integrated in a WDM/MDM system to carry different modes at different wavelengths. Specifically, TE_0 and TE_2 can be carried at 1550 nm, while TE_0 and TE_1 can be carried at 1543 nm. However, this comes with the price of increasing the complexity of the operating system. In addition, the (de) multiplexing function can be transferred to 1310 nm wavelength by applying design equations to that wavelength. Finally, it is clear from the figure that the crosstalks in all cases are always less than –20 dB. We also emphasize that changing the duty cycle and/or tooth width of the Bragg grating can also be used to improve and optimize the IL for the modes. Specifically, making the duty cycle equal 0.2 results in a reduction of the IL of the fundamental mode to 0.5 dB, while other modes' ILs remain the same.

6. EXPERIMENTAL RESULTS

Our device has been fabricated using 100 keV electron beam lithography. A SOI wafer of 200 mm diameter, 220 nm silicon thickness, and 2 μm buffer oxide thickness has been used as the base material for the fabrication. After fabrication, the device has been inspected using a scanning electron microscope (SEM) to verify patterning and etch quality. A 2.2 μm oxide cladding has been deposited using a plasma-enhanced chemical vapor deposition (PECVD) process to protect the functional device.

Spectral responses have been measured using an Agilent 81600B tunable laser source with a wide tuning range (1500–1600 nm) in 10 pm steps. A polarization-maintaining fiber array has been used to couple light in/out of the chip. The fibers have been spaced by 127 μm from each other. To allow automated measurements for the device, all on-chip grating couplers are spaced with the same distance.

A. Circuit Description

Figure 5 shows a schematic of the whole circuit with different parts. The used grating couplers couple light from the fiber to the fundamental mode on a waveguide of width 500 nm. Waveguides with different widths are connected by tapers in order to reduce back reflections and maintain the power in the desired mode. The taper to the right of Fig. 5 is used to
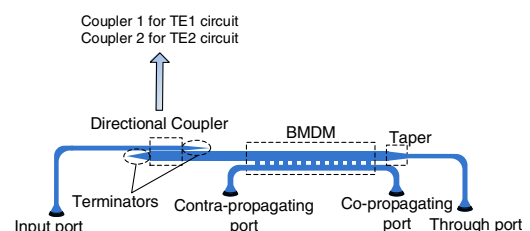

Fig. 4. 3D-FDTD simulations of proposed (de)multiplexer with coupler gap $r = 140$ nm, grating period $\Lambda = 364.4$ nm, and length $L = 30\Lambda$ when excited with: (a) fundamental mode, (b) first-order mode, and (c) second-order mode.

Fig. 5. Schematic diagram of the whole device with different components (not to scale).

allow the detection of the fundamental mode in the 936 nm waveguide via a grating coupler.

We have designed different terminators to end waveguides properly so that the back reflection is minimized (less than –25 dB). The tip of different terminators is 60 nm, which is the minimum feature size of the fabrication process. For the fabricated BMDM, we have used a Bragg grating with a duty cycle of 20% and period of 378 nm. The length of both waveguides is 18 μm with a coupler gap of 192 nm. We have used an indirect calibration method to extract the IL of our BMDM, which depends on reference circuit(s) to eliminate the loss due to irrelevant components. The first is only a grating coupler pair with a waveguide between them, from which we can get the IL of the grating coupler alone. The second is a grating coupler pair with a pair of directional couplers. By comparing the performance of the second reference circuit with the first reference circuit, we get the IL of the one-directional coupler. Finally, we design a circuit with the grating coupler pair, directional coupler, and our proposed BMDM [Fig. 5]. In the last circuit, we know the performance of all components except our BMDM. Subtracting all other components' ILs, we can get the IL of our BMDM.

1. Grating Coupler Pair Layout
The grating coupler pair layout and data are shown in Fig. 6. The two fiber grating couplers are designed for 1550 nm quasi-TE operation. We limit our analysis to the top 10 dB of the grating coupler response to avoid noise introduced at the end of the spectrum. The following analysis is limited to the corresponding wavelength range.

B. Mode Excitation
To provide first- and second-order modes to test our device, we introduce two-directional couplers to couple the input fundamental mode to the desired mode in the 936 nm waveguide. Coupler 1 and 2 can couple the fundamental mode to the first- and second-order modes, respectively. The width of 450 nm has been chosen, instead of the conventional 500 nm, for coupler 1, as it gives the best couple to the first-order mode in the 936 nm waveguide. For coupler 2, we choose the width of 270 nm to couple the fundamental mode to the second-order mode in the desired waveguide, as depicted in the mode chart in Fig. 2. The length and gap values have been obtained through a 3D FDTD simulation sweep to get the best coupling
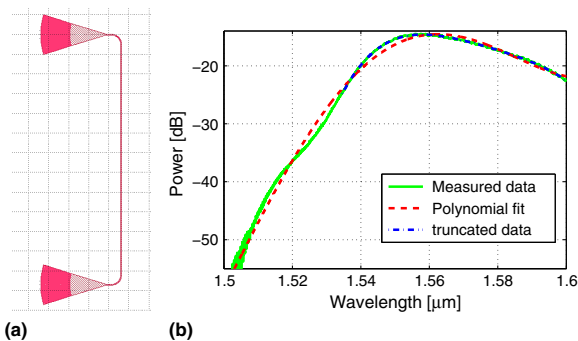
efficiency to the desired mode while agreeing with the shot pitch and minimum feature size of the fabrication process. Figure 5 shows a circuit that has two options. The first is using coupler 1 for TE_0/TE_1 conversion. The second is using coupler 2 for TE_0/TE_2 conversion.

C. Experimental Data
Figure 7 shows the experimental and fitted data for both couplers 1 and 2. The length and gap for coupler 1 are 21 μm and 144 nm, respectively, while they are 12 μm and 174 nm, respectively, for coupler 2. The corresponding ILs for couplers 1 and 2 are –0.8183 dB and –0.6197 dB, respectively, at 1550 nm. The grating couplers used in the fabrication process can inject/detect only the fundamental mode. As a result, the crosstalk to higher order modes cannot be addressed.

The calibration process has been done by subtracting the loss of the grating coupler pair and the used directional coupler from the whole system response. Performing the calibration process, we get the ILs for the fundamental, first-order, and second-order modes, as shown in Fig. 9. Specifically, at 1550 nm, the ILs are –3.127 dB, –1.465 dB, and –2.384 dB, respectively. The crosstalk is less than –21 dB for all modes. Working at a wavelength of 1540 nm can improve the ILs of the fundamental and second-order modes to –2.042 dB and –0.9292 dB, respectively. From Figs. 8 and 9, we can see the similarity between the simulation results and the experimental data in the same wavelength range. The little difference can be attributed to some unavoidable fabrication deviations. Functional Si layer non-uniformity and tilt of
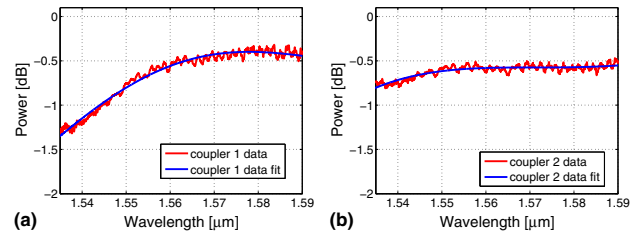

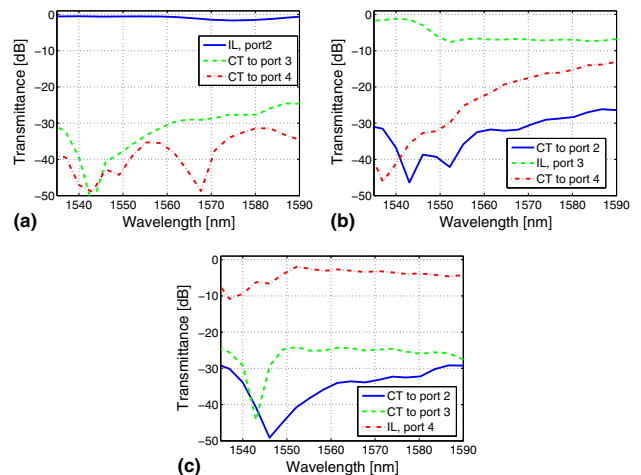**Fig. 7.** Experimental and fitted date for: (a) coupler 1 and (b) coupler 2.

Fig. 8. 3D-FDTD simulation of the fabricated device for (a) fundamental, (b) first-order, and (c) second-order modes.

Fig. 6. (a) Grating coupler pair layout. (b) Measured, fitted, and truncated data.
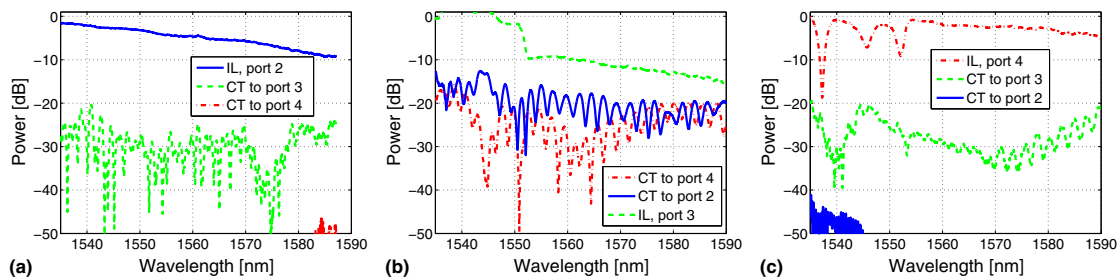
Fig. 9. Measured results for the fabricated device (a) fundamental, (b) first-order, and (c) second-order modes.

Table 1. Comparison with Previous Work

References	Number of Modes	Method	Dimension
[14]	4	MMI	2 mm²
[18,19]	2	Tapered DC	>50 µm, 15.2 µm
[20]	8	6-cascaded DC	>330 µm
[21]	2	Asymmetric Y-jun	>100 µm
[22]	3	Asymmetric Y-jun	>350 µm
[25]	2	MZI	>100 µm
BMDM	3	2-waveguides and Bragg grating	18 µm

the waveguide side walls from the vertical position are a few examples. However, the used theoretical model still gives a good indication for the performance of the fabricated device.

Table 1 provides a comparison between our proposed BMDM with previous MDMs. From this table, we can see the reduction of the size accomplished for our device.

7. CONCLUSION

A compact BMDM with strip waveguides has been proposed, and its performance has been analyzed and simulated. The (de) multiplexer is very compact and can separate/combine three modes (TE_0, TE_1, and TE_2) in a simple and efficient way. Both EIM and coupled-mode theory have been adopted in our mathematical analysis. Simple formulas for both ILs and RLs of all multiplexing modes have been obtained with their dependence on the coupler gap. In addition, approximate closed-form expressions for inter- and intra-waveguide coupling coefficients have been introduced for the strip waveguide. The validity of our developed mathematical model has been verified by 3D FDTD simulations. Numerical results of both the ILs and crosstalks predict good performance of the proposed device. Fabrication results show acceptable ILs and crosstalks for all modes.

REFERENCES

1. M. Schoeberl, F. Brandner, J. Spars, and E. Kasapaki, "A statically scheduled time-division-multiplexed network-on-chip for real-time systems," in *6th IEEE/ACM International Symposium on Networks-on-Chip (NoCS)*, Lyngby, Denmark, 2012, pp. 152–160.
2. H. Ishio, J. Minowa, and K. Nosu, "Review and status of wavelength-division-multiplexing technology and its application," J. Lightwave Technol. **2**, 448–463 (1984).
3. D. J. Richardson, J. M. Fini, and L. E. Nelson, "Space division multiplexing in optical fibres," Nat. Photonics **7**, 354–362 (2013).
4. D. Dai and J. E. Bowers, "Silicon-based on-chip multiplexing technologies and devices for peta-bit optical interconnects," Nanophotonics **3**, 283–311 (2014).
5. T. Yamamoto, K. Tanaka, S. Ide, and T. Aoki, "Optical interconnect technology for high-bandwidth data connection in next-generation servers," Fujitsu Sci. Tech. J. **50**, 117–122 (2014).
6. C. P. Chen, J. B. Driscoll, R. R. Grote, B. Souhan, R. M. Osgood, and K. Bergman, "Mode and polarization multiplexing in a Si photonic chip at 40 Gb/s aggregate data bandwidth," IEEE Photon. Technol. Lett. **27**, 22–25 (2015).
7. T. Rahman, D. Rafique, B. Spinnler, M. Bohn, A. Napoli, C. M. Okonkwo, and H. de Waardt, "38.4 Tb/s transmission of single-carrier serial line-rate 400 Gb/s PM-64 QAM over 328 km for metro and data center interconnect applications," in *Optical Fiber Communications Conference (OFC)*, Anaheim, California, 2016, pp. 1–3.
8. J. Sakaguchi, W. Klaus, J. Manuel, D. Mendinueta, B. J. Puttnam, R. S. Luis, Y. Awaji, N. Wada, T. Hayashi, T. Nakanishi, T. Watanabe, Y. Kokubun, T. Takahata, and T. Kobayashi, "Large spatial channel (36-core/3 mode) heterogeneous few-mode multicore fiber," J. Lightwave Technol. **34**, 93–103 (2016).
9. T. Mizuno, H. Takara, A. Sano, and Y. Miyamoto, "Dense space-division multiplexed transmission systems using multi-core and multi-mode fiber," J. Lightwave Technol. **34**, 582–592 (2016).
10. S. Inao, T. Sato, S. Sentsui, T. Kuroha, and Y. Nishimura, "Multicore optical fiber," in *Optical Fiber Communications Conference (OFC)*, Washington, DC, 1979, paper WB1.
11. S. Matsuo, Y. S. K. Takenaga, Y. Amma, S. Saito, K. Saitoh, T. Matsui, K. Nakajima, T. Mizuno, H. Takara, Y. Miyamoto, and T. Morioka, "High-spatial-multiplicity multicore fibers for future dense space-division-multiplexing systems," J. Lightwave Technol. **34**, 1464–1475 (2016).
12. N. Zhao, X. Li, G. Li, and J. M. Kahn, "Capacity limits of spatially multiplexed free-space communication," Nat. Photonics **9**, 822–826 (2015).
13. H. Qiu, H. Yu, T. Hu, G. Jiang, H. Shao, P. Yu, J. Yang, and X. Jiang, "Silicon mode multi/demultiplexer based on multimode grating-assisted couplers," Opt. Express **21**, 17904–17911 (2013).
14. Y. Kawaguchi and K. Tsutsumia, "Mode multiplexing and demultiplexing devices using multimode interference couplers," Electron. Lett. **38**, 1701–1702 (2002).
15. S. Berdague, "Mode division muliplexing in optical fibers," Appl. Opt. **21**, 1950–1955 (1982).
16. F. Saitoh, K. Saitoh, and M. Koshiba, "A design method of a fiber-based mode multi/demultiplexer for mode-division multiplexing," Opt. Express **18**, 4709–4716 (2010).
17. B. Stern, X. Zhu, C. P. Chen, L. D. Tzuang, J. Cardenas, K. Bergman, and M. Lipson, "On-chip mode-division multiplexing switch," Optica **2**, 530–535 (2015).
18. Y. Luo, Y. Yu, M. Ye, C. Sun, and X. Zhang, "Integrated dual-mode 3 db power coupler based on tapered directional coupler," Sci. Rep. **6**, 23516 (2016).
19. Y. Ding, J. Xu, F. D. Ros, B. Huang, H. Ou, and C. Peucheret, "On-chip two-mode division multiplexing using tapered directional coupler-based mode multiplexer and demultiplexer," Opt. Express **21**, 10376–10382 (2013).

20. J. Wang, P. Chen, S. Chen, Y. Shi, and D. Dai, "Improved 8-channel silicon mode demultiplexer with grating polarizers," Opt. Express **22**, 12799–12807 (2014).

21. J. B. Driscoll, R. R. Grote, B. Souhan, J. I. Dadap, M. Lu, and R. M. Osgood, "Asymmetric Y junctions in silicon waveguides for on-chip mode-division multiplexing," Opt. Lett. **38**, 1854–1856 (2013).

22. W. Chen, P. Wang, T. Yang, G. Wang, T. Dai, Y. Zhang, L. Zhou, X. Jiang, and J. Yang, "Silicon three-mode (de)multiplexer based on cascaded asymmetric Y junctions," Opt. Lett. **41**, 2851–2854 (2016).

23. J. Wang, Y. Xuan, M. Qi, H. Huang, Y. Li, M. Li, X. Chen, Z. Sheng, A. Wu, W. Li, X. Wang, S. Zou, and F. Gan, "Broadband and fabrication-tolerant on-chip scalable mode-division multiplexing based on mode-evolution counter-tapered couplers," Opt. Lett. **40**, 1956–1959 (2015).

24. W. Chen, P. Wang, and J. Yang, "Mode multi/demultiplexer based on cascaded asymmetric Y-junctions," Opt. Express **21**, 25113–25119 (2013).

25. D. Prez-Galacho, D. Marris-Morini, A. Ortega-Monux, J. G. Wanguemert-Prez, and L. Vivien, "Add/drop mode-division multiplexer based on a Mach–Zehnder interferometer and periodic waveguides," IEEE Photon. J. **7**, 7800907 (2015).

26. T. Mulugeta and M. Rasras, "Silicon hybrid (de)multiplexer enabling simultaneous mode and wavelength-division multiplexing," Opt. Express **23**, 943–949 (2015).

27. M. Ye, Y. Yu, C. Sun, and X. Zhang, "On-chip data exchange for mode division multiplexed signals," Opt. Express **24**, 528–535 (2016).

28. L. F. Frellsen, Y. Ding, O. Sigmund, and L. H. Frandsen, "Topology optimized mode multiplexing in silicon-on-insulator photonic wire waveguides," Opt. Express **24**, 16866–16873 (2016).

29. H. M. H. Shalaby, "Bi-directional coupler as a mode-division multiplexer/demultiplexer," J. Lightwave Technol. **34**, 3633–3640 (2016).

30. J. Davis, A. Grieco, M. C. Souza, and Y. Fainman, "Grating-assisted counter-directional resonators for on-chip mode conversion," in *CLEO: Science and Innovations*, San Jose, California (Optical Society of America, 2017), paper SF1J.4.

31. Z. Lu, H. Yun, Y. Wang, Z. Chen, F. Zhang, N. Jaeger, and L. Chrostowski, "Broadband silicon photonic directional coupler using asymmetric-waveguide based phase control," Opt. Express **23**, 3795–3806 (2015).

32. M. Dumitrescu and M. Guina, "Effective index method for computation of the propagation constant and electromagnetic field distribution in z-uniform dielectric or semiconductor waveguides," in *5th Conference on Optics*, Bucharest, Romania, 1997, pp. 922–925.

33. H. Furuta, H. Noda, and A. Ihaya, "Novel optical waveguide for integrated optics," Appl. Opt. **13**, 322–326 (1974).

34. R. K. Varshney and A. Kumar, "A simple and accurate modal analysis of strip-loaded optical waveguides with various index profiles," J. Lightwave Technol. **6**, 601–606 (1988).

35. K. S. Chiang, "Analysis of the effective index method for the vector modes of rectangular core dielectric waveguides," IEEE Trans. Microw. Theory Tech. **44**, 692–700 (1996).

36. M. Qiua, "Effective index method for heterostructure-slab-waveguide-based two-dimensional photonic crystals," Appl. Phys. Lett. **81**, 1163–1165 (2002).

37. A. Yariv, "Coupled-mode theory for guided-wave optics," IEEE J. Quantum Electron. **9**, 919–933 (1973).

38. E. Peral and A. Yariv, "Supermodes of grating-coupled multimode waveguides and application to mode conversion between copropagating modes mediated by backward Bragg scattering," J. Lightwave Technol. **17**, 942–947 (1999).

39. E. Palik, *Handbook of Optical Constants of Solids* (Academic, 1998).